

Constraints on Planets in Nearby Young Moving Groups Detectable by High-Contrast Imaging and Gaia Astrometry

A. L. Wallace¹★, M. J. Ireland¹†, C. Federrath¹

¹Research School of Astronomy & Astrophysics, Australian National University, Canberra, ACT 2611, Australia

Accepted XXX. Received YYY; in original form ZZZ

ABSTRACT

The formation of giant planets is best studied through direct imaging by observing planets both during and after formation. Giant planets are expected to form either by core accretion, which is typically associated with low initial entropy (cold-start models) or by gravitational instability, which corresponds to a high initial entropy of the gas (hot-start models). Thus, constraining the initial entropy provides insight into the planet formation mechanism and determines the resultant brightness evolution. We find that, by observing planets in nearby moving groups of known age both through direct imaging and astrometry with Gaia, it will be possible to constrain the initial entropy of giant planets. We simulate a set of planetary systems in stars in nearby moving groups identified by BANYAN Σ and assume a model for planet distribution consistent with radial velocity detections. We find that Gaia should be able to detect approximately 50% of planets in nearby moving groups greater than $\sim 0.3 M_J$. Using 5σ contrast limits of current and future instruments, we calculate the flux uncertainty, and using models for the evolution of the planet brightness, we convert this to an initial entropy uncertainty. We find that, for future instruments such as MICADO and METIS on E-ELT and VIKING with VLTI, the entropy uncertainty is less than $0.5 k_B/\text{baryon}$, showing that these instruments should be able to distinguish between hot and cold-start models.

Key words: gaseous planets – formation – detection

1 INTRODUCTION

Direct imaging of exoplanets is an important tool in understanding the formation and evolution of giant planets. There has been some progress with discovering planets in the process of formation (e.g., PDS 70b; [Keppler et al. \(2018\)](#)) however, recent surveys of the nearest star-forming regions, despite discoveries of new brown dwarf companions, failed to detect planetary-mass companions ([Kraus & Ireland 2011](#); [Wallace et al. 2020](#)). It has also been determined that current instruments have insufficient sensitivity at the expected separations to detect planets around solar-type stars in nearby star-forming regions ([Wallace & Ireland 2019](#)). However, there has been greater success with wider-separation planets around higher-mass stars in young nearby moving groups such as β -Pictoris ([Lagrange et al. 2009](#)) and 51-Eridani ([Macintosh et al. 2015](#)).

Moving groups are nearby collections of stars that have the same age and similar motions through space. These have been studied in detail over the years ([Torres et al. 2008](#); [Zuckerman et al. 2011](#); [Rodriguez et al. 2013](#)) and recent precise proper motion and parallax measurements of nearby stars have allowed reasonably accurate determination of membership to these groups ([Gagné et al. 2018](#); [Schneider et al. 2019](#)). There are at least 27 such associations within 150 pc with ages less than ~ 800 Myr. The young ages and small dis-

tances of these systems make them ideal for young planet surveys ([López-Santiago et al. 2006](#)).

The upcoming Gaia DR3 and subsequent data releases come with the promise of high-precision mass calculations for many giant, long-period exoplanets ([Perryman et al. 2014](#)). The end-of-mission sensitivity is predicted at $\sim 10 \mu\text{as}$, which means that, for a $1 M_\odot$ star, Gaia can detect a $0.5 M_J$ planet at 100 mas with 20% mass uncertainty. However, Gaia’s expected 10 year mission lifetime puts an upper limit on the semi-major axes of Gaia-detectable planets with non-degenerate solutions. In order to conduct high-contrast imaging studies of Gaia-detectable planets, we must look at young planets in nearby systems.

Planets in the process of formation radiate with a luminosity proportional to their accretion rate and total mass ([Zhu 2015](#)). After formation, planets cool and fade over time, but the rate of cooling depends on their mass and formation conditions ([Spiegel & Burrows 2012](#)). If during formation, the accretion shock radiates all accretion energy away, this is called a cold-start model. If none of the accretion energy is radiated away, it is a hot-start model ([Berardo et al. 2017](#)). Hot and cold-start models are defined by the planet’s initial entropy, the value of which depends on planet mass (as shown in the ‘tuning fork’ diagram in [Marley et al. \(2007\)](#)).

The brightness evolution of a planet depends greatly on its initial entropy. Hot-start planets are generally larger than cold-start planets. During formation, hot-start planets are fainter than cold-start planets, but after formation, they are brighter. Hot-start planets also cool and fade more rapidly than cold-start planets ([Spiegel & Burrows 2012](#)).

★ E-mail: alexander.wallace@anu.edu.au

† E-mail: michael.ireland@anu.edu.au

Thus, as the planets age, the brightness gap between hot and cold-start models will narrow. If we observe young planets of known mass and age, we can use the observed flux to determine the initial entropy of directly imaged planets (Marleau & Cumming 2014).

If the mass and age of a planet is known with reasonable precision, the greatest uncertainty comes from the observed flux. This flux uncertainty depends on the sensitivity of our instruments. In this study, we consider current instrument such as NIRC2, NaCo, SPHERE and GRAVITY and future instruments such as JWST, VIKING (interferometric instrument using VLTI), MICADO on the VLT and METIS on the E-ELT. These instruments have observed and theoretical detection limits which we convert to a flux uncertainty. Using models linking flux, mass and age to initial entropy, we convert this to an entropy uncertainty to determine how well the initial entropy can be constrained.

The rest of the paper is organised as follows. Section 2 summarises our stellar and planet sample and models for the evolution of planet luminosity and its dependence on entropy. Section 3 focuses on detection limits of astrometry and direct imaging and Section 4 presents the numbers of detectable planets in our sample by both methods. Section 5 explains how we can constrain the initial entropy of planets if we know the mass, magnitude and age. Our conclusions are presented in Section 6.

2 STELLAR AND PLANETARY PROPERTIES

2.1 Stellar Sample

The target stars for our simulations are taken from nearby, young (<800 Myr) moving groups. The stars originally come from Gaia’s second data release (DR2) (Brown et al. 2018) and are then sorted into nearby young moving groups. The stars from the Gaia sample also include proper motion measurements and most (~70 %) include radial velocity values. This initial sample included stars across the entire sky within 70 pc, brighter than a G-magnitude of 13 and temperature greater than 3800 K. Beyond ~70 pc the majority of giant planets in ~10 year orbits are not detectable and moving group knowledge is incomplete. Stars cooler than 3800 K are no-longer considered solar-type and have a measured smaller fraction of planets (Johnson et al. 2007).

The Gaia sample is then passed into the BANYANΣ algorithm presented in Gagné et al. (2018) to determine moving group membership. This algorithm uses each star’s celestial coordinates, distance and proper motion values and associated errors to determine the probability of membership to a particular moving group from a list of 27 possible groups. Our sample of stars within 70 pc, indicating association membership is shown in Figure 1. We have included all stars with membership probability greater than 95 %.

As shown in the sky map, there are only 10 moving groups with stars closer than 70 pc. Our target stars are spread across the sky, but the majority is in the southern hemisphere. The Argus association has the highest number of targets, but the existence of this group has been controversial (Bell et al. 2015), as it was unclear whether it represented a single moving group. Recent studies have suggested the association does indeed exist with an age of 40–50 Myr (Zuckerman 2018), so we include it in our study.

2.2 Planet Distribution

For the distribution of planets, we assume a broken power law in mass M and period P from Fernandes et al. (2019), which has the

functional form

$$\frac{d^2N}{d\ln M d\ln P} = CM^\alpha P^\beta, \quad (1)$$

where N is the number of planets per star and C is a normalisation constant. The mass power law is approximately consistent across all masses with $\alpha = -0.45$. Based on radial velocity detections, the period power law changes with distance from the star with $\beta > 0$ at short periods and $\beta < 0$ for long periods. Fernandes et al. (2019) gives several different values, but in this study we use the symmetric distribution in which $\beta = 0.63$ for periods less than 860 days and $\beta = -0.63$ for periods greater than 860 days. The constant C is set such that the total number of planets matches observations. In the symmetric distribution from Fernandes et al. (2019), $C = 0.067$.

We apply this distribution in terms of semi-major axis a rather than period. This means the power-law index becomes 0.945 at small separations and -0.945 at wide separations. The power law changes at a semi-major axis of 1.77 au for a $1 M_\odot$ star. This distribution implies the majority of planets are low mass and at small separations. While there have been high-mass planets observed at wide separations around HR 8799, β -Pic and 51 Eri, these are around high-mass stars where there is known to be an excess of high-mass planets (Johnson et al. 2010). Most of our targets are of near solar mass, and for simplicity, we are not modifying our planetary distribution as a function of mass. We regard these relatively rare wide-separation planets as a separate population for which Gaia observations are not feasible due to their long orbital periods.

We simulate planet masses over a range of 0.3–13 M_J and semi-major axes over a range of 1–100 au. Integrating the power law shown in Equation 1 over this range gives $N \sim 0.08$ planets per star. The symmetric planet distribution from Fernandes et al. (2019) is shown in Figure 2. Period is converted to semi-major axis by assuming a $1 M_\odot$ star.

2.3 Planet Luminosity and Magnitude

When giant planets form, they emit radiation as a result of accretion energy and are at their brightest during the period of runaway accretion (Lissauer et al. 2009). After formation, the luminosity declines with age and is mostly dependant on the planet’s mass and entropy.

The luminosity as a function of age is shown in Figure 3 for planets of varying mass and entropy of $9.5 k_B/\text{baryon}$ (blue curves) and $10.5 k_B/\text{baryon}$ (red curves) using hot and cold-start models from Spiegel & Burrows (2012). This is calculated from applying the Stefan-Boltzmann Law to the radius and temperature plots in Figure 5 of their paper and interpolating between their initial entropies. In order to determine planet detectability, a more useful quantity is the absolute magnitude of a planet in near-infrared bands. As in Figure 3, we calculate magnitude evolution using models from Spiegel & Burrows (2012), taking the magnitudes from their Figure 7 and interpolating between initial entropies. Some example magnitude evolution curves are shown in Figure 4 for the K ($2.2\mu\text{m}$) and L’ ($3.77\mu\text{m}$) bands using the same initial entropies as Figure 3. The cooling curves in Figures 3 and 4 demonstrate how, at old ages, the difference between luminosities or magnitudes for different initial entropy declines. However, at the young ages (~10 Myr) we consider in this study, there is a noticeable difference between the two entropies for high-mass planets, which indicates we should be able to constrain the formation models of massive (> 2 M_J) planets.

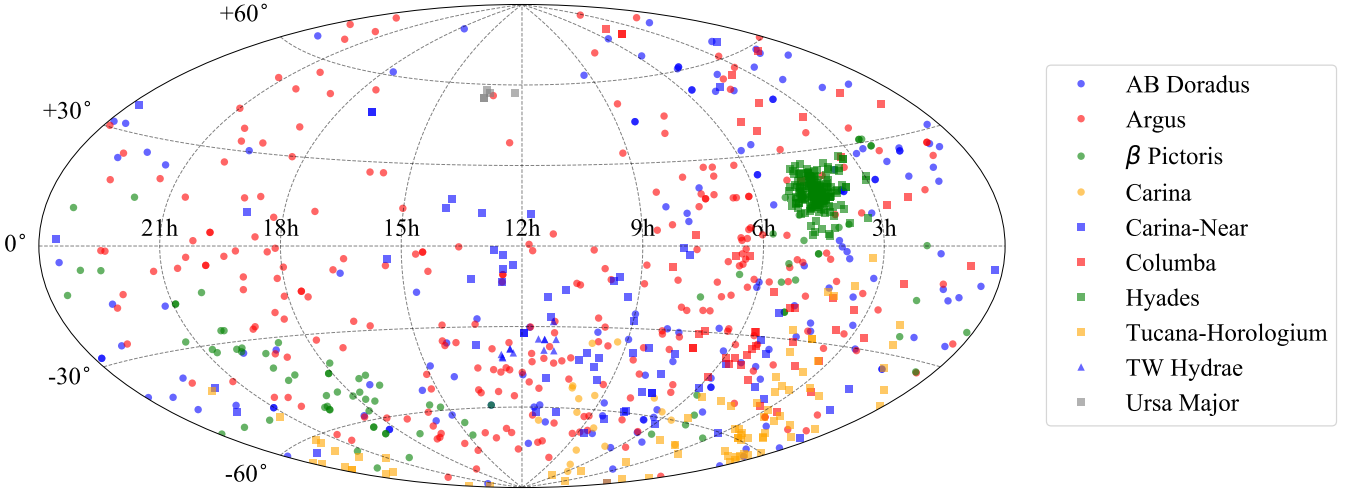


Figure 1. Stars in our sample that belong to a moving group determined by BANYANΣ. Map is shown in celestial coordinates with East to the left.

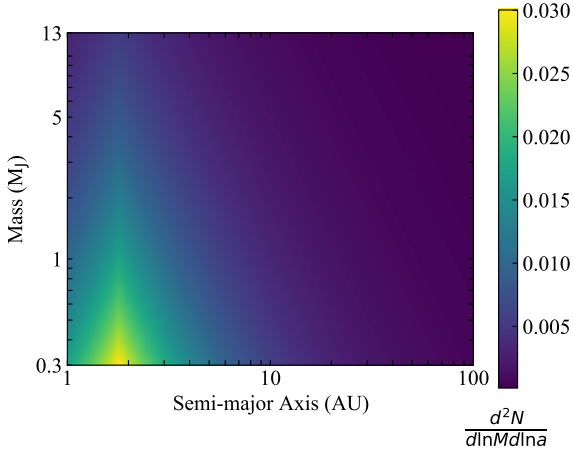


Figure 2. The differential mass and semi-major axis distribution of our simulated planets from [Fernandes et al. \(2019\)](#). Integrating this across our simulation range gives $N = 0.08$ planets per star.

3 PLANET DETECTABILITY

3.1 Detection by Gaia Astrometry

The upcoming Gaia data releases are expected to have improved astrometry measurements of stars and have the potential to discover exoplanets through this method. As a planet orbits its star, the planet's gravity causes the star to move back and forth over the course of an orbit. The angular size of this motion in arcseconds is given by

$$\alpha = \left(\frac{M_p}{M_\star} \right) \left(\frac{a_p}{d_\star} \right), \quad (2)$$

where M_p and M_\star are the masses of the planet and star, respectively, a_p is the semi-major axis of the planet in au and d_\star is the distance to the star in pc. Gaia has the potential to detect this small motion with an estimated uncertainty of $10 \mu\text{as}$ ([Perryman et al. 2014](#)). In this study, we consider a potential Gaia detection as genuine if the relative uncertainty is less than 25%. Thus, if we set the relative

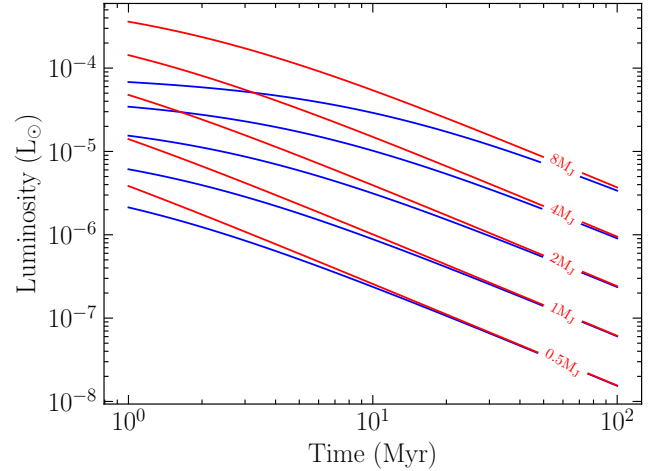


Figure 3. Evolution of planet luminosity for different planet masses and initial entropies. The blue curves represent initial entropy of $9.5 k_B/\text{baryon}$ and red represents $10.5 k_B/\text{baryon}$. This is calculated using the temperature and radius curves from Figure 5 in [Spiegel & Burrows \(2012\)](#), applying the Stefan-Boltzmann Law and interpolating between entropies shown in their paper.

uncertainty in α ,

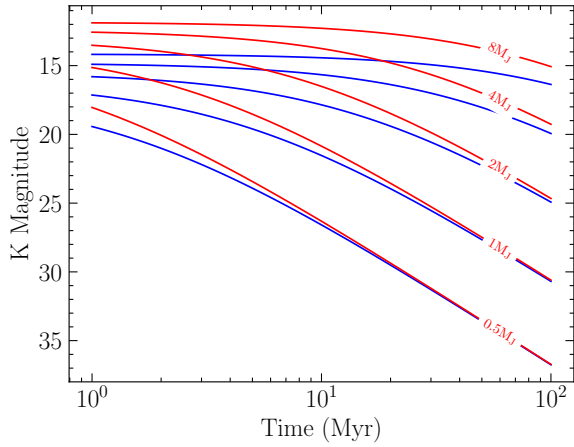
$$\frac{\sigma_\alpha}{\alpha} = \sigma_\alpha \left(\frac{M_\star}{M_p} \right) \left(\frac{d_\star}{a_p} \right) < 0.25, \quad (3)$$

we can rearrange to get a mass limit,

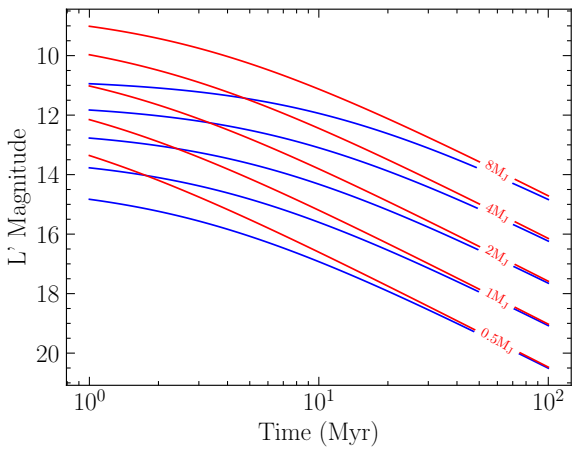
$$M_p > 4 \sigma_\alpha \left(\frac{M_\star d_\star}{a_p} \right). \quad (4)$$

For example, assuming $\sigma_\alpha = 10 \mu\text{as}$, for a $1 M_\odot$ star 50 pc away and a planet 5 au away from its star, Gaia can detect planets greater than $0.4 M_J$. This indicates that Jupiter analogues should be easily detectable by Gaia.

Gaia is also limited by the expected length of its mission. If we assume that Gaia can detect planets by observing only 1/3 of a period



(a) Absolute Magnitude in K Band



(b) Absolute Magnitude in L' Band

Figure 4. Evolution of planet magnitude in the K band (panel a) and in the L' band (panel b) for different planet masses and initial entropies. The blue curves represent initial entropy of $9.5 k_B/\text{baryon}$ and red represents $10.5 k_B/\text{baryon}$. This is based on the curves in Figure 7 of Spiegel & Burrows (2012) and, as before, we interpolate between entropies.

with a mission lifetime of 10 years, it cannot detect planets with a period greater than 30 years.

3.2 Detection by Direct Imaging

Planets are detected through a variety of direct imaging techniques. A common method is angular differential imaging (ADI), in which multiple images of a star are captured at different times and rotated to a common orientation to remove any instrumental artefacts (Marois et al. 2006). Another method is reference star differential imaging (RDI), in which the image of a nearby star is subtracted from the target image, leaving behind possible planetary mass companions (Lafreniere et al. 2007).

Most directly imaged planets were detected using a coronagraph, which blocks out the light of the star. However, this presents problems when searching for planets at small separations. Indirect methods such as kernel phase have shown great promise at small separations (Martinache 2010). Even without detecting planets, these methods give us insight into the detection capabilities.

The detection limits for various instruments are shown in Figure 5,

Table 1. Apparent magnitude limits of instruments considered in this paper. Note that for most targets, the contrast and not these background limits most influences detectability.

Instrument	K Mag. Limit	L' Mag. Limit
SPHERE	22.5	-
GRAVITY	19.5	-
MICADO	29.5	-
VIKING (UTs)	23.2	18.5
VIKING (ATs)	19.9	15.3
NIRC2	-	17.94
NaCo	-	18.55
METIS	-	21.8
JWST	-	23.8

assuming a bright target. These limits were determined by observations or, in the case of future instruments, simulated performance. The SPHERE and MICADO limits come from Perrot et al. (2018). The GRAVITY limit is based on the lower limits of the curves in Abuter et al. (2019), assuming a 1 hour integration time. The NaCo limits come from Quanz et al. (2012) and the METIS limits are based on Carlomagno et al. (2016). The NIRC2 limit comes from our contrast limit through recent observations of Taurus (Wallace et al. 2020), which are consistent with vortex coronagraph reference star differential imaging limits (Xuan et al. 2018). The JWST limit is adapted from Beichman et al. (2010). The VIKING limits for L' come directly from the model by Martinache & Ireland (2018), assuming that the companions must be resolved in the kernel null maps, and with a loss in contrast as the planets approach the edge of the telescope PSF (at separations of $0.5\text{--}0.8\lambda/D$). The assumed contrast of 4×10^{-5} at $5\text{-}\sigma$ assumes either 80 nm RMS fringe tracking errors and 10% intensity fluctuations, or 120 nm RMS fringe tracking errors and 2% intensity fluctuations. The VIKING limits for K are based on a more optimistic, but theoretically possible set of assumptions. For observations with the UTs, fringe tracking up to $0.5''$ off-axis is assumed with an RMS fringe tracking RMS error of 30 nm. The contrast limit shown is the magnitude difference between the faintest detectable planet and its star in the K and L' bands.

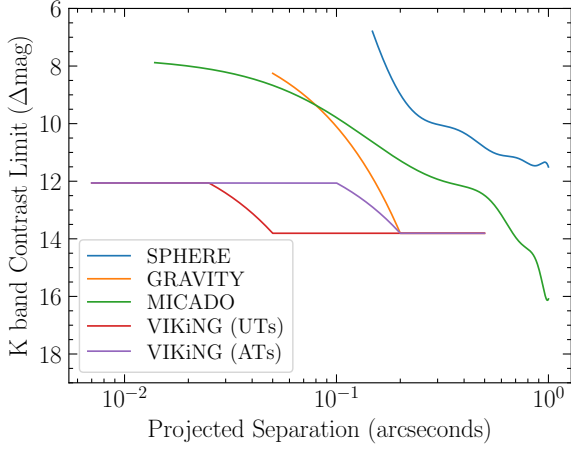
The apparent background-limited magnitude limits of these instruments are shown in Table 1, which apply mostly to faint targets. A planet is detectable if it is brighter than both the magnitude limit and the contrast limit shown in Figure 5.

4 SIMULATED DETECTABLE PLANETS

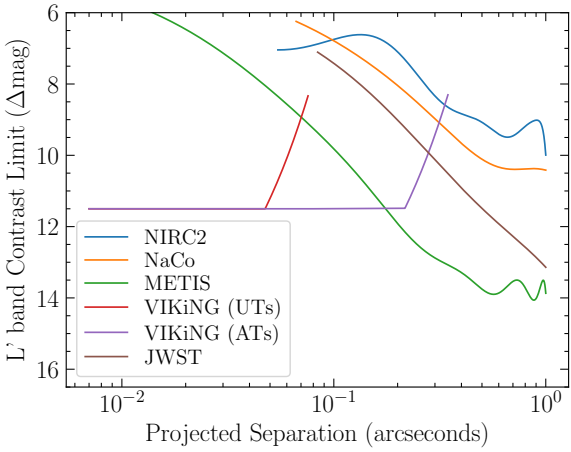
For each star in our sample shown in Section 2.1, we simulate a set of planet systems using the power-law distribution shown in Section 2.2. This simulation was run 5000 times per star, but only $\sim 8\%$ of these simulations produced planets (as explained in Figure 2.)

4.1 Planets Detectable by Gaia DR 3

Using our simulated sample of planets around stars in nearby moving groups, we calculated how many can be detected by Gaia. As explained in Section 3.1, Gaia's expected lifetime of 10 years limits the orbital periods of detectable planets. We are optimistically assuming Gaia can detect a planet from $1/3$ of an orbit so this excludes planets with orbital periods greater than 30 years. Using the mass limit shown in Equation 4 and applying the angular resolution from Perryman et al. (2014), we assume Gaia can detect all remaining planets above this mass limit. After running the simulation 100 times,



(a) K band



(b) L' band

Figure 5. Assumed limits for current and future instruments as a function of separation. See text for detailed assumptions.

the average number of planets per group and the average number detectable by Gaia are shown in Table 2.

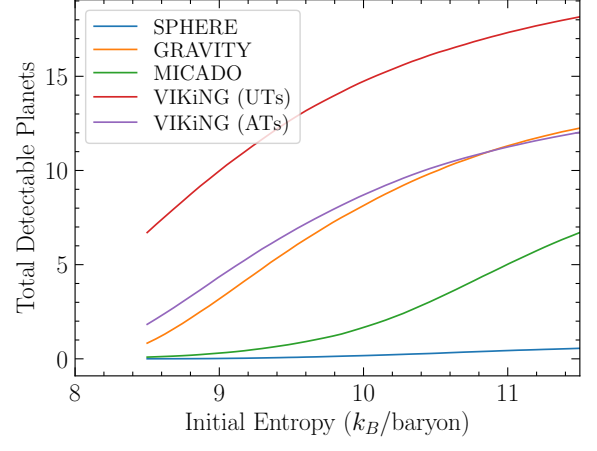
We have 1753 stars in our sample across all groups shown in Table 2 and, on average, we simulate 142.6 giant planets ($M > 0.3 M_J$) across all groups. This agrees with the integral of our distribution of ~ 0.08 planets per star. Our estimates suggest that Gaia is able to detect 87.3 planets, which is slightly more than half of our sample.

4.2 Planets detectable by both Gaia and Direct Imaging

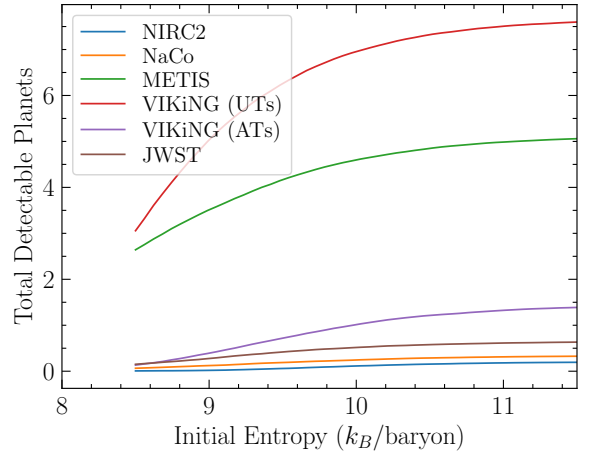
Using planetary cooling curves shown in Figure 4 and the limits of current and future instruments shown in Figure 5, we can determine how many Gaia-detectable planets are also detectable by high-contrast imaging. To calculate this, we need the age and the initial entropy of each simulated planet.

We assume the age is the same as the moving group age listed in Table 2, and we assume a range of initial planet entropies from 8.5–11.5 k_B/baryon . This gives us a set of magnitudes for every planet in our sample. The numbers of detectable planets for each instrument are shown in Figure 6.

As shown in Figure 6, MICADO, GRAVITY, METIS and VIKiNG



(a) K band



(b) L' band

Figure 6. Total number of planets detectable by both Gaia DR 3 and high contrast imaging across all moving groups.

should be able to detect more than one planet that is also detectable by Gaia, if a survey of nearby moving groups were conducted.

5 CONSTRAINING THE INITIAL ENTROPY

Even if we can detect a young exoplanet through direct imaging, this does not necessarily constrain formation models. In this section, we present a simulated set of detected planets with brightness and mass uncertainties, and determine whether observations can constrain the formation entropy.

5.1 Entropy Uncertainty

We start by simulating a set of planets detectable by Gaia as shown in Table 2. These planets are all assigned a mass and semi-major axis according to the distribution presented in Figure 2 and age equal to the age of its moving group. The initial entropy of these planets is unknown. The likelihood of a particular entropy given our simulated data, $L(S|D)$, is derived from Bayes Theorem,

$$L(S|D) \propto P(D|S)P(S), \quad (5)$$

Table 2. Total number of simulated planets in each group and number detectable by Gaia. In our model, there are approximately 0.08 planets with mass greater than 0.3 M_J per star and Gaia can detect approximately half of these.

Group Name	Age (Myr)	Average Distance (pc)	Number of Stars	Average Number of Planets	Average Number of Detectable Planets
AB Doradus	149^{+51}_{-19}	43.19	367	29.87	18.99
Argus	45 ± 5	48.33	630	51.28	30.37
β Pictoris	22 ± 6	39.60	149	12.10	7.88
Carina	45^{+11}_{-7}	49.22	26	2.15	1.30
Carina-Near	~ 200	34.28	148	12.00	8.28
Columba	42^{+6}_{-4}	47.47	79	6.45	3.78
Hyades	750 ± 100	46.67	239	19.38	11.16
Tucana-Horologium	45 ± 4	49.34	94	7.67	4.51
TW Hydrae	10 ± 3	53.68	21	1.71	1.02

where $P(D|S)$ is the probability of the data for a given entropy and $P(S)$ is the prior probability of that entropy. The probability $P(D|S)$ is calculated for a range of entropies S_i and is approximately given by

$$P(D|S_i) \propto e^{-\frac{(f-f_i)^2}{2\sigma_f^2}}, \quad (6)$$

where f is the planet's flux given an input entropy S and f_i is the flux for each entropy S_i . The flux error, σ_f , can be calculated from the contrast limits of various instruments shown in Figure 5. These are 5σ contrast limits which can be converted to flux limits using the flux of the star. The flux error is then simply this value divided by 5. For simplicity, we assume all values of entropy are equally possible and assume a flat distribution for $P(S)$.

The likelihood shown in Equation 5 is used to calculate the entropy distribution for a single planet. If we simulate multiple planets, the likelihood functions are simply multiplied together. The likelihood is then given by

$$L(S|D) = \prod_{i=1}^N L(S|D_i), \quad (7)$$

where D_i is the data for a single planet in the simulation and N is the total number of planets in the simulation.

As an example, we consider a star of apparent magnitude 7 in the K and L' bands at a distance of 40 pc and age of 50 Myr. Assuming a true entropy of $9.5 k_B/\text{baryon}$, the likelihood as a function of modelled entropy is shown in Figure 7 for both wavelength bands using MICADO in the K band and METIS in the L' band. The solid curves are planets at 10 au and the dashed curves are at 20 au. The likelihood curves in Figure 7 confirm that the initial entropy of a $2 M_J$ planet cannot be constrained by either instrument, while a $4 M_J$ planet has a likelihood curve narrow enough for the entropy to be constrained by METIS, but not quite by MICADO. The entropy uncertainty of this sample of 4 planets is calculated from the standard deviation of the curves multiplied together.

Applying this method to a random sample of Gaia-detectable planets, we determine the combined entropy uncertainty for a range of input entropies for different instruments. The result for METIS, VIKING and JWST is shown in Figure 8. The curves in Figure 8 demonstrate that, for 'warm'-start planets (entropy of $9-10 k_B/\text{baryon}$) the entropy uncertainty is within $0.5 k_B/\text{baryon}$ for MICADO, METIS and VIKING in both K and L' bands. This indicates that these instruments should be able to distinguish between hot- and cold-start models for planets in nearby moving groups. We note that, unlike the other instruments, VIKING is still only at a feasibility study level at this point.

6 CONCLUSIONS

In this paper, we have examined the brightness evolution of giant planets and the dependence on initial entropy. Given that high-entropy planets are brighter than low-entropy planets of similar mass but this difference becomes less at old ages. If we observe planets at young ages, it should be possible to constrain initial entropy.

Using the expected uncertainty for Gaia astrometry from Perryman et al. (2014), we determine that Gaia should be able to detect more than 50% of giant planets in nearby moving groups and calculate their mass. Combining this with the estimated ages of these moving groups, we can use the detected flux to determine the initial entropy. We performed this over a simulated sample of planets around existing stars in nearby moving groups, assuming a symmetric planet distribution from Fernandes et al. (2019).

We used the measured and expected 5σ contrast limits for current and future instruments to estimate the expected flux error on the planets in our simulated sample. We found that future instruments MICADO and METIS have the best contrast levels at wide angles, while interferometers GRAVITY and VIKING are best at small angles. However, we note that improvements to GRAVITY, known as GRAVITY+ are currently being implemented and, of the VIKING concepts, only the L' concept has significant funding. Overall, assuming Gaia can detect giant planets in nearby moving groups, we find that these future instruments should also be able to detect some planets, if we were to conduct a survey of nearby moving groups.

We can use the instrumental flux error, combined with the estimated ages and masses from Gaia, to constrain the formation entropy of directly imaged planets. We found that MICADO, GRAVITY, METIS and VIKING should be able to constrain the formation entropy of planets more massive than $\sim 3 M_J$ to within $0.5 k_B/\text{baryon}$. This implies that these instruments should be able to distinguish between planets formed by hot and cold-starts.

DATA AVAILABILITY

The data underlying this article are available from the corresponding author on reasonable request.

ACKNOWLEDGEMENTS

We thank Mark Krumholz for initiating the discussions of planet entropy which led to this work. This research was supported by the Australian Government through the Australian Research Council's Discovery Projects funding scheme (DP190101477).

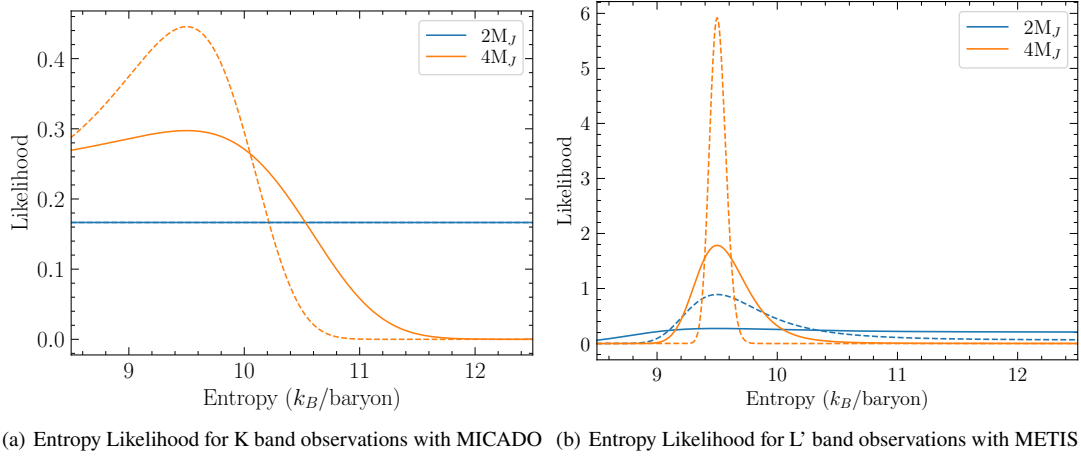


Figure 7. Likelihood of entropy for given data in K and L' bands, with MICADO and METIS respectively, assuming an input entropy of $9.5 k_B/\text{baryon}$. The solid curves are planets at 10 au and the dashed curves are planets at 20 au.

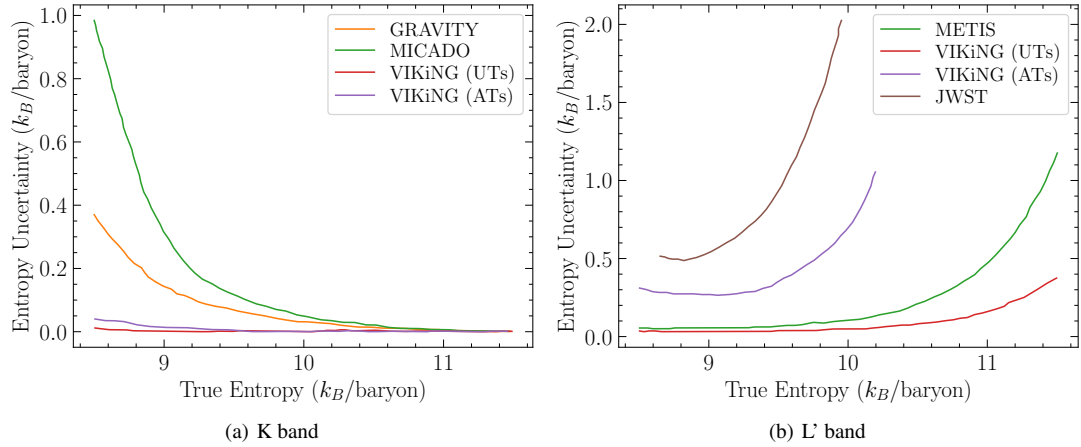


Figure 8. Entropy Uncertainty as a function of input entropy. The horizontal axis is an assumed entropy which translates to an observed brightness and the vertical axis is the resultant width of the combined entropy distribution as shown in Figure 7. For most instruments, the entropy uncertainty is below $0.5 k_B/\text{baryon}$ which is less than the difference between hot and cold-start models. This implies we should be able to distinguish between the two models.

References

- Abuter R., et al., 2019, *Eso Messenger*
- Beichman C. A., et al., 2010, *Publications of the Astronomical Society of the Pacific*, 122, 162
- Bell C. P., Mamajek E. E., Naylor T., 2015, *Monthly Notices of the Royal Astronomical Society*, 454, 593
- Berardo D., Cumming A., Marleau G.-D., 2017, *The Astrophysical Journal*, 834, 149
- Brown A., et al., 2018, *Astronomy & astrophysics*, 616, A1
- Carlomagno B., et al., 2016, in *Adaptive Optics Systems V*. p. 990973
- Fernandes R. B., Mulders G. D., Pascucci I., Mordasini C., Emsenhuber A., 2019, *The Astrophysical Journal*, 874, 81
- Gagné J., et al., 2018, *The Astrophysical Journal*, 856, 23
- Johnson J. A., Butler R. P., Marcy G. W., Fischer D. A., Vogt S. S., Wright J. T., Peek K. M., 2007, *The Astrophysical Journal*, 670, 833
- Johnson J. A., Aller K. M., Howard A. W., Crepp J. R., 2010, *Publications of the Astronomical Society of the Pacific*, 122, 905
- Kepler M., et al., 2018, *Astronomy & Astrophysics*, 617, A44
- Kraus A. L., Ireland M. J., 2011, *The Astrophysical Journal*, 745, 5
- Lafreniere D., Marois C., Doyon R., Nadeau D., Artigau É., 2007, *The Astrophysical Journal*, 660, 770
- Lagrange A.-M., et al., 2009, *Astronomy & Astrophysics*, 493, L21
- Lissauer J. J., Hubickyj O., D'Angelo G., Bodenheimer P., 2009, *Icarus*, 199, 338
- López-Santiago J., Montes D., Crespo-Chacón I., Fernández-Figueroa M., 2006, *The Astrophysical Journal*, 643, 1160
- Macintosh B., et al., 2015, *Science*, 350, 64
- Marleau G.-D., Cumming A., 2014, *Monthly Notices of the Royal Astronomical Society*, 437, 1378
- Marley M. S., Fortney J. J., Hubickyj O., Bodenheimer P., Lissauer J. J., 2007, *The Astrophysical Journal*, 655, 541
- Marois C., Lafreniere D., Doyon R., Macintosh B., Nadeau D., 2006, *The Astrophysical Journal*, 641, 556
- Martinache F., 2010, *The Astrophysical Journal*, 724, 464
- Martinache F., Ireland M. J., 2018, *arXiv preprint arXiv:1802.06252*
- Perrot C., Baudoz P., Boccaletti A., Rousset G., Huby E., Clénet Y., Durand S., Davies R., 2018, *arXiv preprint arXiv:1804.01371*
- Perryman M., Hartman J., Bakos G. Á., Lindgren L., 2014, *The Astrophysical Journal*, 797, 14
- Quanz S. P., Crepp J. R., Janson M., Avenhaus H., Meyer M. R., Hillenbrand L. A., 2012, *The Astrophysical Journal*, 754, 127
- Rodríguez D. R., Zuckerman B., Kastner J. H., Bessell M., Faherty J. K., Murphy S. J., 2013, *The Astrophysical Journal*, 774, 101

- Schneider A. C., Shkolnik E. L., Allers K. N., Kraus A. L., Liu M. C., Weinberger A. J., Flagg L., 2019, *The Astronomical Journal*, 157, 234
 Spiegel D. S., Burrows A., 2012, *The Astrophysical Journal*, 745, 174
 Torres C. A., Quast G. R., Melo C. H., Sterzik M. F., 2008, arXiv preprint arXiv:0808.3362
 Wallace A., Ireland M., 2019, *Monthly Notices of the Royal Astronomical Society*, 490, 502
 Wallace A., et al., 2020, *Monthly Notices of the Royal Astronomical Society*, 498, 1382
 Xuan W. J., et al., 2018, *AJ*, 156, 156
 Zhu Z., 2015, *The Astrophysical Journal*, 799, 16
 Zuckerman B., 2018, *The Astrophysical Journal*, 870, 27
 Zuckerman B., Rhee J. H., Song I., Bessell M., 2011, *The Astrophysical Journal*, 732, 61

This paper has been typeset from a $\text{\TeX}/\text{\LaTeX}$ file prepared by the author.